RSC Advances

PAPER

View Article Online
View Journal | View Issue

Check for updates

Cite this: *RSC Adv.*, 2019, **9**, 31497

Low pH constructed Co(II) and Ni(II) 1D coordination polymers based on C_α-substituted analogues of zoledronic acid: structural characterization, and spectroscopic and magnetic properties†

Tomasz Rojek, *[a] Waldemar Goldeman, [a] Katarzyna Ślepokura, [b]
Marek Duczmal,[a] Agnieszka Wojciechowska [a] and Ewa Matczak-Jon [a]

Received 22nd July 2019
Accepted 24th September 2019

DOI: 10.1039/c9ra05673d

rsc.li/rsc-advances

Three novel coordination compounds based on α,α-disubstituted analogues of zoledronic acid with a cyclopropane (cpp) or cyclobutane (cbt) ring on the C_α carbon, isomorphous $[Co(H_2cppZol)(H_2O)]\cdot H_2O$ (**1a**), $[Ni(H_2cppZol)(H_2O)]\cdot H_2O$ (**1b**) and $[Co(H_2cbtZol)(H_2O)]\cdot H_2O$ (**2a**), were synthesized under hydrothermal conditions at low pH. Single-crystal X-ray diffraction analysis revealed that all the compounds had a 1D double zig–zag chain architecture with an 8 + 8 ring motif formed by alternately arranged symmetrical $(-O-P-O-)_2$ bridges linking equivalent octahedral metal centres. Both the ligand coordination mode and chain architecture displayed by **1a**, **1b** and **2a** are unique among 1D $[M(H_2L)(H_2O)_x]\cdot yH_2O$ coordination polymers based on nitrogen-containing bisphosphonates reported so far. All the compounds exhibit similar decomposition pathways upon heating with thermal stabilities decreasing in the order **1b** > **1a** > **2a**. The IR spectra revealed that lattice water release above 227, 178 and 97 °C, respectively, does not change the chain architecture leaving them intact up to *ca.* 320, 280 and 240 °C. Magnetic behaviour investigations indicated that **1a**, **2a** and **1b** exhibit weak alternating antiferromagnetic–ferromagnetic exchange interactions propagated between the magnetic centres through double $(-O-P-O-)_2$ bridges. The boundary between antiferro- and ferromagnetic couplings for the Co–O⋯O–Co angle in **1a** and **2a** was estimated to be *ca.* 80°. This value is also applicable for recently reported $[M_3(HL)_2(H_2O)_6]\cdot 6H_2O$ (M = Co, Ni) complexes based on α,α-disubstituted analogues of zoledronic acid and can be used to the explain magnetic behaviour of **1b**.

1. Introduction

Organophosphonic acids are a class of ligands widely known for their excellent affinity for metal ions. The propensity to coordinate and bridge various metal centres resulting from multiple O-donor atoms occurring in tetrahedral phosphonic/phosphonate group(s) allows them to form coordination compounds with diverse supramolecular architectures[1] and promising applications in the field of catalysis,[2] gas storage,[3] biotechnology,[4] photoluminescence[5] or magnetism.[6] Therefore, metal-organophosphonate solids belong to an important and extensively developed class of functional materials.

Among a wide range of organophosphonate ligands, special attention has been concentrated on the family of $H_2O_3P-C(R_1)(R_2)-PO_3H_2$ bisphosphonic acids (BPs), which due to presence of geminal phosphonic groups attached to the carbon atom can capture a large number of metal ions simultaneously. Moreover, using various synthesis conditions and/or introducing donor-rich functional groups in R_1 and/or R_2 positions allows them to control both nuclearity and dimensionality of metal-bisphosphonate materials.[7] This can be primarily realized by controlling the pH-dependent protonation state of phosphonate and other functional groups of ligand. In addition, other factors such as the nature and geometry of selected metal centre, steric strain imposed by R_1/R_2 substituents as well as an introduction of auxiliary ligands have significant impact on the architecture of desired compounds.[8] To achieve pure phase materials, hydrothermal technique is commonly used in the synthesis of BPs-based coordination compounds. Therefore, careful determination of appropriate reaction conditions such as: metal-to-ligand stoichiometric ratio, temperature or reaction time also play a significant role.

---

[a] *Department of Chemistry, Wrocław University of Science and Technology, Wybrzeże Wyspiańskiego 27, 50-370 Wrocław, Poland. E-mail: ewa.matczak-jon@pwr.edu.pl*

[b] *Faculty of Chemistry, University of Wrocław, Joliot-Curie 14, 50-383 Wrocław, Poland*

† Electronic supplementary information (ESI) available. CCDC 1940766–1940768. For ESI and crystallographic data in CIF or other electronic format see DOI: 10.1039/c9ra05673d

To explore and expand the area of metal-BPs coordination compounds we have focused our research on new derivatives of zoledronic acid, H_4Zol (Scheme 1). This compound is a member of N-containing bisphosphonates family (NBPs), currently considered to be the most potent agent in the treatment of bone diseases[9] and successfully exploited as multidentate ligand suitable for a synthesis of various metal complexes.[10] With the aim to determine how structural modifications of H_4Zol imply topologies and architectures of coordination compounds formed with d-block metal ions, we synthesized a series of its derivatives with sterically demanding substituents on C_α atom, such as methyl groups (H_4dmtZol), a cyclopropane (H_4cppZol), cyclobutane (H_4cbtZol) or cyclopentane (H_4cptZol) ring.[11] All the ligands were structurally characterized[12,13] and examined for their ability to interact with Co(II) and Ni(II) under different pH conditions. Our recent studies have demonstrated that at pH *ca.* 4.0–5.0, both cations form one-dimensional coordination polymers with a general formula $M_3(HL)_2(H_2O)_6\cdot 6H_2O$ (M = Co(II), Ni(II), HL = HdmtZol^{3-}, M = Co(II), HL = HcppZol^{3-}, HcbtZol^{3-})[12–14] or $M_3(HL)_2(H_2O)_4\cdot 2H_2O$ (M = Co(II), HL = HcptZol^{3-}),[13] featuring alternately arranged $[M2_2(HL)(H_2O)_2]_2$ entities and $\{M1O_6\}$ octahedrons with crystallographically and spectroscopically distinct M2 and M1 centres. In contrast, less sterically hindered HZol^{3-} ligand tends to form under similar conditions 2D and 3D coordination networks.[15]

In this article we show that carrying the reaction at lower pH affords diverse systems architecture. By reacting Co(II) or Ni(II) chlorides with H_4cppZol (**1**) or H_4cbtZol (**2**) (Scheme 1) under hydrothermal conditions at 2.5–3.5 pH range we synthesized a series of 1D coordination polymers: isomorphous $[Co(H_2cppZol)(H_2O)]\cdot H_2O$ (**1a**), $[Ni(H_2cppZol)(H_2O)]\cdot H_2O$ (**1b**) and $[Co(H_2cbtZol)(H_2O)]\cdot H_2O$ (**2a**).

The search in the Cambridge Structural Database (CSD)[16] has revealed almost twenty crystal structures of similar 1D $[M(H_2L)(H_2O)_x]\cdot yH_2O$ ($x = 0$–1, $y = 0$–3) coordination polymers based on various NBPs. (Table S1, ESI†). Among them, d-block metal complexes of the type $[M(H_2L)]\cdot xH_2O$ ($x = 0$–3; M = Cd(II), Zn(II), Mn(II), Co(II), Cu(II), H_2L^{2-} = 2-(4-pyridinyl)-1-hydroxyl-1,1-ethylidenediphosphonate;[17] M = Mn(II), Cd(II), H_2L^{2-} = risedronate;[18] M = Mn(II), Cu(II), H_2L^{2-} = pamidronate;[19] M = Mn(II), H_2L^{2-} = alendronate,[20] zoledronate[21]) and $[M(H_2L)(H_2O)]$ (M = Fe(II), Co(II), Mn(II), H_2L^{2-} = risedronate[22]) have been found to reveal the ladder chain architecture. Commonly, in this type of structures, phosphonate μ_2-O bridges link two equivalent metal centres into a four-membered $(MO)_2$ dinuclear unit, whereas phosphonate O–P–O bridges connect adjacent dinuclear units to form eight-membered $(M–O–P–O)_2$ rings resulting in double 1D infinite chain. It is to note, that formation of such 4 + 8 rings motif along the coordination chain is favoured regardless of varying geometries and nature of metal centres[17–22] as well as subtle differences in ligands coordination modes (Fig. S1a–d, ESI†).[22] The double zig–zag chain architecture is characteristic for Ca(II) complexes. The four-membered ring motif generated by μ_2-O bridges between metal centres is propagated along double chains displayed by seven-coordinate $[Ca(H_2Pam)(H_2O)]\cdot H_2O$ and $[Ca(H_2Zol)(H_2O)]$ (Fig. S2a, ESI†)[23]. On the other hand, six-coordinate $[Ca(H_2Ale)]\cdot H_2O$ complex represents the structure, in which a combination of phosphonate O–P–O and μ_2-O bridges between metal centres leads to 6 + 6 rings motif propagated along the coordination chain (Fig. S2b, ESI†).[24]

Herein, we report the structures of **1a**, **1b** and **2a** determined by single-crystal X-ray diffraction and their detailed characterization with the use of TG-DTA, DSC, FT-IR, NIR-UV/Vis techniques and magnetic susceptibility measurements. Interestingly, both ligands coordination mode and chains architecture of the reported compounds are unique among NBPs-based $[M(H_2L)(H_2O)_x]\cdot yH_2O$ coordination polymers reported so far.

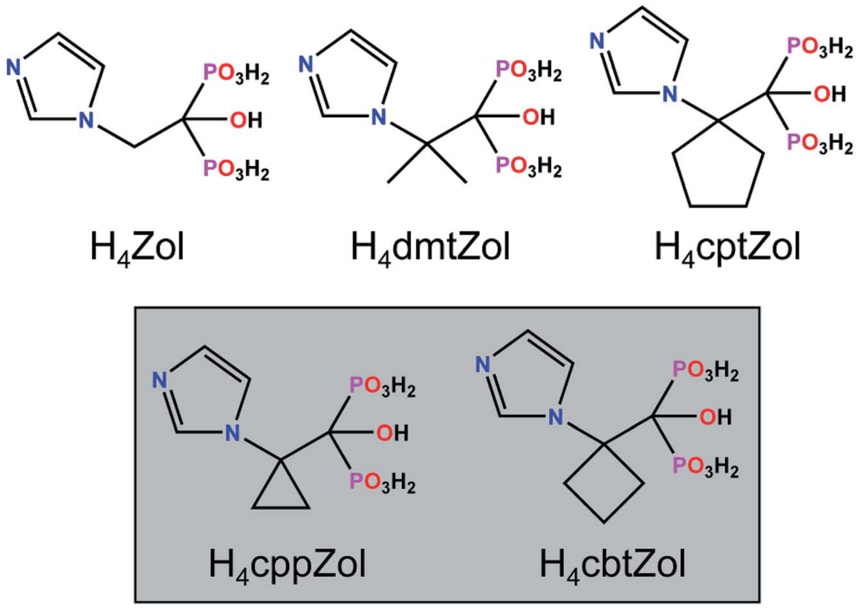

Scheme 1 Zoledronic acid and its α,α-disubstituted analogues.

2. Experimental

2.1 Materials

All commercially available reagents and solvents were used as received without further purification. 1-Hydroxy-2-[1-(1*H*-imidazol-1-yl)cyclopropyl]ethylidene-1,1-diphosphonic acid (H_4cppZol) and 1-hydroxy-2-[1-(1*H*-imidazol-1-yl)cyclobutyl] ethylidene-1,1-diphosphonic acid (H_4cbtZol) were synthesized according to previously described procedure.[11] Details of synthesis and purity confirmation of both ligands are reported in ref. 12 and 13.

2.2 Synthesis of Co(H_2cppZol)(H_2O)·H_2O (1a)

H_4cppZol (0.10 mmol, 0.0298 g) and $CoCl_2\cdot 6H_2O$ (0.05 mmol, 0.0119 g) were dissolved in water (5 ml). Then, the pH of the reaction mixture was adjusted to 2.5 by 1 M NaOH. The obtained clear and pink solution was sealed in a glass tube and heated at 100 °C for 72 h. After the reaction system had been cooled slowly to room temperature, pink crystals of **1a** were isolated, washed with distilled water and dried at room temperature. Crystals were collected as a monophasic material based on the powder XRD (Fig. S3, ESI†). Yield 16.4 mg (41.6% based on H_4cppZol). Elemental anal. found (calc.) for $C_7H_{14}CoN_2O_9P_2$ (%): C, 21.70 (21.49); H, 3.31 (3.61); N, 7.09 (7.16). IR (ATR, cm^{-1}): 3605 br & w, 3356 br & w, 3145 w, 3043 br & w, 2936 br & w, 1659 w, 1620 w, 1582 w, 1534 w, 1461 w, 1424 w, 1398 w, 1348 w, 1216 w, 1196 w, 1172 w, 1161 w, 1120 m, 1071 s, 1048 s, 1020 s, 1001 s, 977 m, 946 s, 901 m, 888 s, 874 s, 845 s, 804 m, 791 m, 770 m, 700 m, 655 s, 631 m, 614 s, 560 s, 544 s, 528 s, 488 s, 465 s, 449 s, 410 s.

2.3 Synthesis of Ni(H_2cppZol)(H_2O)·H_2O (1b)

H_4cppZol (0.10 mmol, 0.0298 g) and $NiCl_2\cdot 6H_2O$ (0.07 mmol, 0.0167 g) were dissolved in water (5 ml). Then, the pH of the reaction mixture was adjusted to 2.9 by 1 M NaOH. The obtained clear and green solution was sealed in a glass tube and heated at 100 °C for 72 h. After the reaction system had been cooled slowly to room temperature, green crystals of **1b** were isolated, washed with distilled water and dried at room temperature. Crystals were collected as a monophasic material based on the powder XRD (Fig. S4, ESI†). Yield 11.6 mg (29.5% based on H_4cppZol). Elemental anal. found (calc.) for $C_7H_{14}NiN_2O_9P_2$ (%): C, 21.66 (21.51); H, 3.40 (3.62); N, 7.01 (7.17). IR (ATR, cm^{-1}): 3606 br & w, 3350 br & w, 3146 w, 3042 br & w, 2933 br & w, 1644 w, 1620 w, 1582 w, 1533 w, 1460 w, 1426 w, 1401 w, 1347 w, 1218 w, 1195 w, 1175 w, 1162 w, 1125 m, 1070 s, 1048 s, 1020 s, 1000 s, 945 s, 890 s, 849 s, 808 m, 793 m, 772 m, 701 m, 654 s, 631 m, 615 s, 546 s, 529 s, 488 s, 468 s, 450 s, 415 s.

2.4 Synthesis of Co(H_2cbtZol)(H_2O)·H_2O (2a)

H_4cbtZol (0.10 mmol, 0.0312 g) and $CoCl_2\cdot 6H_2O$ (0.10 mmol, 0.0238 g) were dissolved in water (5 ml). Then, the pH of the reaction mixture was adjusted to 3.5 by 1 M NaOH. The obtained clear and pink solution was sealed in a glass tube and heated at 100 °C for 72 h. After the reaction system had been cooled slowly to room temperature, pink crystals of **2a** were isolated, washed with distilled water and dried at room temperature. Crystals were collected as a monophasic material based on the powder XRD (Fig. S5, ESI†). Yield 21.3 mg (52.2% based on H_4cbtZol). Elemental anal. found (calc.) for $C_8H_{16}CoN_2O_9P_2$ (%): C, 23.74 (23.71); H, 3.61 (3.99); N, 6.80 (6.92). IR (ATR, cm^{-1}): 3600 br & w, 3526 br & w, 3360 br & w, 3176 w, 3151 w, 3119 w, 3057 br & w, 3033 br & w, 3001 br & w, 2966 br & w, 1653 w, 1609 w, 1584 w, 1534 w, 1480 w, 1465 w, 1443 w, 1386 w, 1354 w, 1319 w, 1276 w, 1230 w, 1203 w, 1179 m, 1128 w, 1089 s, 1063 s, 1038 s, 1013 s, 986 s, 948 s, 872 s, 837 s, 786 m, 771 m, 741 m, 655 s, 629 m, 604 s, 537 s, 511 s, 467 s, 439 s.

2.5 X-ray crystallography

Crystallographic measurements for **1a**, **1b** and **2a** were performed on κ-geometry diffractometer Agilent Technologies Xcalibur R with a Ruby CCD camera and with graphite monochromatized MoKα radiation at 110, 100 and 80 K, respectively, using an Oxford Cryosystems cooler. Data collection, cell refinement, data reduction and analysis as well as analytical absorption correction were carried out with CrysAlisPro.[25] The crystal structures of **1b** and **2a** were solved with direct methods using SHELXS-97 (ref. 26) and refined on F^2 by a full-matrix least squares technique with SHELXL-2014 (ref. 27) with anisotropic thermal parameters for all the ordered non-H atoms. As complex **1a** is isomorphous with **1b**, the refinement was started by using the coordinates of heavy (non-H) atoms taken from **1b** and further refined as described above.

H atoms in **1a**, **1b** and **2a** were found in difference Fourier maps and were refined isotropically. In the final refinement cycles, all C-bound H atoms, as well as N-bound H atoms in **1a** and **1b**, were repositioned in their calculated positions and refined using a rigid model, with C–H = 0.95–0.99 Å, N–H = 0.88 Å, and with $U_{\mathrm{iso}}(\mathrm{H}) = 1.2U_{\mathrm{eq}}(\mathrm{C, N})$. The H atoms of hydroxyl group in **1a**, **1b** and **2a**, phosphonate group in **2a** and all attached to water molecules were refined with the O–H bond lengths restrained to 0.840(2) Å and with $U_{\mathrm{iso}}(\mathrm{H}) = 1.5U_{\mathrm{eq}}(\mathrm{O})$. Then the AFIX 147 and AFIX 3 riding models were used to constrain phosphonate H atoms in **1a**, **1b** and **2a**. Additionally, the H⋯H distances in the water molecules were restrained to 1.360(2) or 1.380(2) Å in **1a**, **1b** or **2a**, respectively. N-bound H atom in **2a** was refined with the N–H distance restrained to 0.880(2) Å and with $U_{\mathrm{iso}}(\mathrm{H}) = 1.2U_{\mathrm{eq}}(\mathrm{N})$. Then, it was constrained to ride on its parent N atom (AFIX 3 instruction).

Crystallographic data and structure refinement parameters are summarized in Table 1 and the crystallographic information files (CIFs) deposited at the Cambridge Crystallographic Data Centre (CCDC no. 1940766–1940768) and provided as ESI.† All figures were made using the DIAMOND program.[28]

2.6 Powder X-ray diffraction analysis

PXRD data were collected on a Bruker D8-Advance diffractometer equipped with a VÅNTEC-1 detector ($\lambda_{\mathrm{CuK}\alpha} = 1.5418$ Å). The

Table 1 Crystal data and structure refinement for compounds **1a**, **1b** and **2a**

Compound	**1a**	**1b**	**2a**
CCDC no.	1940766	1940767	1940768
Chemical formula	$C_7H_{14}CoN_2O_9P_2$	$C_7H_{14}N_2NiO_9P_2$	$C_8H_{16}CoN_2O_9P_2$
M_r	391.07	390.85	405.10
Crystal system	Triclinic	Triclinic	Monoclinic
Space group	$P\bar{1}$	$P\bar{1}$	$C2/c$
a (Å)	7.848(3)	7.816(3)	13.666(4)
b (Å)	7.886(3)	7.849(3)	8.447(2)
c (Å)	10.880(5)	10.849(4)	22.247(5)
α (°)	90.97(3)	91.03(3)	
β (°)	93.60(3)	93.26(3)	94.45(3)
γ (°)	114.95(3)	114.92(3)	
V (Å^3)	608.6(5)	602.0(4)	2560.4(11)
T (K)	110	100	80
Z	2	2	8
D_c (g cm^{-3})	2.134	2.156	2.102
μ (mm^{-1})	1.73	1.93	1.65
Crystal size (mm)	0.12 × 0.04 × 0.04	0.12 × 0.01 × 0.01	0.27 × 0.06 × 0.02
Diffractometer	Agilent Technologies, Xcalibur R, Ruby	Agilent Technologies, Xcalibur R, Ruby	Agilent Technologies, Xcalibur R, Ruby
Absorption correction	Analytical	Analytical	Analytical
T_{min}, T_{max}	0.855, 0.941	0.873, 0.973	0.796, 0.969
Radiation type	Mo Kα	Mo Kα	Mo Kα
Wavelength (Å)	0.71073	0.71073	0.71073
F(000)	398	400	1656
Refl. measured	16 719	5948	9127
Refl. independent	5098	3636	3029
Refl. observed [$I > 2\sigma(I)$]	3840	1815	2510
No. of parameters	192	192	200
No. of restrains	7	133	9
R_{int}	0.038	0.062	0.027
$(\sin\theta/\lambda)_{max}$ (Å^{-1})	0.679	0.605	0.680
$R[F^2 > 2\sigma(F^2)]$	0.033	0.042	0.032
w$R(F^2)$	0.064	0.060	0.075
S	0.93	0.70	1.04
$\Delta\rho_{max}$, $\Delta\rho_{min}$ (e Å^{-3})	0.51, −0.59	0.84, −0.75	0.49, −0.57

equipment was operated at 30 kV and 40 mA, and data were collected at room temperature in the range of $2\theta = 5$–$50°$.

2.7 ATR FT-IR measurements

The ATR FT-IR (ATR is attenuated total reflectance) spectra were recorded on a Bruker Vertex 70v Fourier transform IR spectrometer equipped with a diamond ATR cell. The spectral data were collected at room temperature over the range 4000–400 cm^{-1} with a resolution of 4 cm^{-1}. Instrument control and initial data processing were performed using OPUS software (v. 7.0 Bruker Optics, Ettlingen, Germany).

2.8 Thermal analysis

Thermogravimetric analysis (TG-DTA) was carried out using a Setaram SETSYS 16/18 analyzer, operating under a nitrogen atmosphere, with a heating rate of 5 K min^{-1} in the range 303–1273 K (sample mass of 10.3, 8.6 and 11.0 mg for **1a**, **1b** and **2a**, respectively). Differential Scanning Calorimetry (DSC) measurements were performed on a Setaram DSC 92 instrument. Samples (3.2–7.0 mg) were contained in alumina pans in the presence of air as the furnace atmosphere. Measurements were performed from ambient temperature up to 219, 314, 387, 457 and 600 °C for **1a**, 284, 352, 529 and 600 °C for **1b** and 175, 329, 525 and 600 °C for **2a** with a heating rate of 5 K min^{-1}.

2.9 NIR-UV/Vis-spectroscopic studies

The NIR-UV/Vis diffuse-reflectance electronic spectra of **1a**, **1b**, **2a** and ligands **1** and **2** were measured on a Cary 500 Scan spectrophotometer over the range 5000–50 000 cm^{-1} with measure step of 10 cm^{-1} at room temperature. The spectra were recorded with identical parameters as a white reference sample. To obtain the band positions of components of d–d bands in the spectra of cobalt(II) (**1a**, **2a**) and nickel(II) (**1b**) complexes the variable digital method[29] was used with the following parameters: step = 20 cm^{-1}, $\alpha = 400$ and $N = 40$ (**1a**); step = 20 cm^{-1}, $\alpha = 400$ and $N = 30$ (**2a**); and step = 20 cm^{-1}, $\alpha = 500$, $N = 40$ (**1b**).

2.10 Magnetic measurements

Magnetic susceptibility in the temperature range from 1.7 to 300 K in a field of 100 mT (**1a** and **2a**) or 500 mT (**1b**) and magnetization up to 5 T were measured with a Quantum Design SQUID magnetometer. Diamagnetic corrections (-202×10^{-6}, -212×10^{-6} and -202×10^{-6} emu mol^{-1} for **1a**, **2a** and **1b**, respectively) were calculated using Pascal's constants. The exchange Hamiltonian in the form $H = -JS_1S_2$ was used consistently throughout the paper. All values of magnetization and magnetic susceptibility are reported per mole of metal.

3. Results and discussion

3.1 Syntheses of 1a, 1b and 2a

Compounds **1a**, **1b** and **2a** were synthesized through hydrothermal reaction at 100 °C for 72 h. However, despite their similarity, obtaining pure phase, the best yield and the highest crystals quality required each reaction to proceed under specific conditions.

Compounds **1a** and **1b** were synthesized with the use of H_4cppZol and $CoCl_2 \cdot 6H_2O$ or $NiCl_2 \cdot 6H_2O$ salts. The highest yields and qualities of crystalline products were achieved in a narrow pH range 2.4–2.6 for **1a** and 2.8–3.0 for **1b**. The decrease in pH below the optimum value resulted in reduction of yield without product deterioration. The increase of pH up to *ca.* 3.5 lead to increase of the reaction yield accompanied by significant deterioration of **1a** and **1b** while in the pH range 3.5–4.0 minor amount of previously reported $Co_3(HcppZol)_2(H_2O)_6 \cdot 6H_2O$[12] or unrecognized green amorphous solid were observed, respectively. Regardless of the reaction pH, the excess of ligand was desirable. It was found that optimum H_4cppZol : Co(II)/Ni(II) molar ratios to obtain pure phases of **1a** and **1b** are 2–1.5 : 1 and 1.5 : 1, respectively. The use of stoichiometric amount of reagents or an excess of metal salt resulted in deterioration of crystals quality and reduction of reaction yield even if the most appropriate pH was reached.

The most favourable pH to obtain optimal crystallinity and reaction yield of **2a** is *ca.* 3.0–4.0. Additionally, both stoichiometric amount of reagents or an excess of ligand (H_4cbtZol : Co(II) molar ratio 1.5–1 : 1) can be used. At pH below 3.0, the decrease of yield without negative impact on product quality was observed while a mixture of **2a** and unidentified, pink, amorphous impurities were obtained above pH 4.0.

The most appropriate for the synthesis of **1a**, **1b** and **2a** are Co(II) and Ni(II) chloride salts. Additionally, **2a** can be obtained when cobalt(II) chloride is replaced by sulphate salt. Attempts to prepare **1a**, **1b** and **2a** by using Co(II)/Ni(II) acetates were unsuccessful.

3.2 Crystal structures of 1a, 1b and 2a

The isomorphous compounds **1a**, **1b** crystallize in triclinic $P\bar{1}$, and **2a** in monoclinic $C2/c$ space group as one-dimensional coordination polymers. Table 1 summarizes all crystal data and structure refinement parameters. Selected geometrical parameters and proposed hydrogen bonds are collected in Tables S2–S4 (ESI†).

The asymmetric units of **1a**, **1b** and **2a** consist of one M1 centre (M1 = Co(II) in **1a** and **2a** or Ni(II) in **1b**), one coordinated H_2L^{2-} ligand ($H_2L^{2-} = H_2cppZol^{2-}$ in **1a** and **1b** or $H_2cbtZol^{2-}$ in **2a**), one coordinated and one lattice water molecule. In all the compounds, the central atom adopts slightly distorted octahedral geometry with equatorial sites occupied by O2, O7 $O4^{i/iii}$ and O1W atoms and axial sites filled by O6, and $O1^{ii/iv}$ atoms (Fig. 1 and S6, ESI†). The average equatorial and axial M1–O distances calculated based on data from Table S3 (ESI†), of 2.118 and 2.059 Å in **1a**, 2.097 and 2.048 Å in **1b** and 2.152 and 2.054 Å in **2a**, result in tetragonality distortion T index defined as $T = R_{int}/R_{out}$ (R_{int} and R_{out} are the average in-plane and out-of-plane M–O (M = Co, Ni) distances[30]) of 1.03, 1.02 and 1.05, respectively, thus indicating slight compression of octahedrons along the axial O2–M1–$O4^{i/iii}$ bond.

In all **1a**, **1b** and **2a**, coordinated ligands contain protonated imidazole N atom, one fully deprotonated and one monoprotonated phosphonate group yielding the overall charge −2. The values of N1–C2–C1–O7 dihedral angles of 165.1(2)°, 165.3(4)° and −172.7(2)°, respectively, (Table S2, ESI†) clearly demonstrate the same *ap* conformation of coordinated $H_2cppZol^{2-}/H_2cbtZol^{2-}$ ligands, recently demonstrated to be rare among NBP's and their anions within coordination compounds and salts.[31] In such arrangement, each ligand exhibits a preference for chelating-bridging mode donating five oxygen atoms to coordinate three M1 (M1 = Co(II)/Ni(II)) ions. The phosphonate O2, O6 and hydroxyl O7 atoms coordinate one M1 centre in a tridentate fashion whereas phosphonate O1 and O4 are involved in monodentate binding of two symmetry related $M1^{ii/iv}$ and $M1^{i/iii}$. The O5 and protonated O3 atoms remain uncoordinated (Fig. S7, ESI†). As a consequence, the pair of M1 and $M1^{i/iii}$ ions is connected through O4–P2–O6 phosphonate bridges from two equivalent ligands to form dinuclear $[M1(H_2L)(H_2O)]_2$ unit with puckered, eight-membered $(M1–O–P–O)_2$ ring and $M1\cdots M1^{i/iii}$ distance within the ring of 4.850(3) Å in **1a**, 4.797(3) Å in **1b** and 4.822(2) Å in **2a**. The O1–P1–O2 bridges extend dinuclear units into infinite zig–zag double chain running along [110] crystallographic direction in **1a** and **1b** or along *b* axis in **2a**. As a result another eight-membered ring with $M1\cdots M1^{ii/iv}$ distance of 4.841(3) Å in **1a** and **1b** and 4.859(2) Å in **2a** is formed (Fig. S8, ESI†). The O7–H7$\cdots O6^{i/iii}$ intermolecular hydrogen bond provides additional stabilization of coordination chain (Fig. 2a, S9a and S10a, ESI†). The chains are extended into 2D hydrogen bonded layer by means of N2–H2N$\cdots O5^{vii/x}$ interaction (Fig. 2b, S9b and S10b, ESI†) and further connected into 3D supramolecular network through O1W–H1W$\cdots O6^{ix/xii}$ and O1W–H2W$\cdots O2^{ix/xii}$ hydrogen bonds between coordinated water molecule and phosphonate oxygen atoms with formation of $R_2^2(6)$ ring motif. Additional stabilization of the supramolecular architecture in **1a** and **1b** is provided by O2W–H3W$\cdots O5^{ix}$ and O2W–H4W$\cdots O1^{ii}$ interactions involving O2W lattice water molecules as hydrogen donors (Fig. 2c, S9c and S10c, ESI†).

Both ligands binding mode and resulting 8 + 8 rings motif propagated along 1D coordination chains are unique among structures of 1D $[M(H_2L)(H_2O)_x] \cdot yH_2O$ ($x = 0–1$, $y = 0–3$) coordination polymers based on NBP ligands reported so far (Table S1, ESI†). Somewhat similar behaviour is only noted for the $[Zn(H_2Ris)]$ complex.[32] However, the fulfilment of both metal and ligand requirements to achieve optimal geometry and energetics leads to tetrahedral geometry maintained by Zn(II) and hydroxyl group of H_2Ris^{2-} remaining uncoordinated (Table S1, ESI†). As a result, eight-membered $(Zn–O–P–O)_2$ dinuclear units being common with **1a**, **1b** and **2a** are extended through

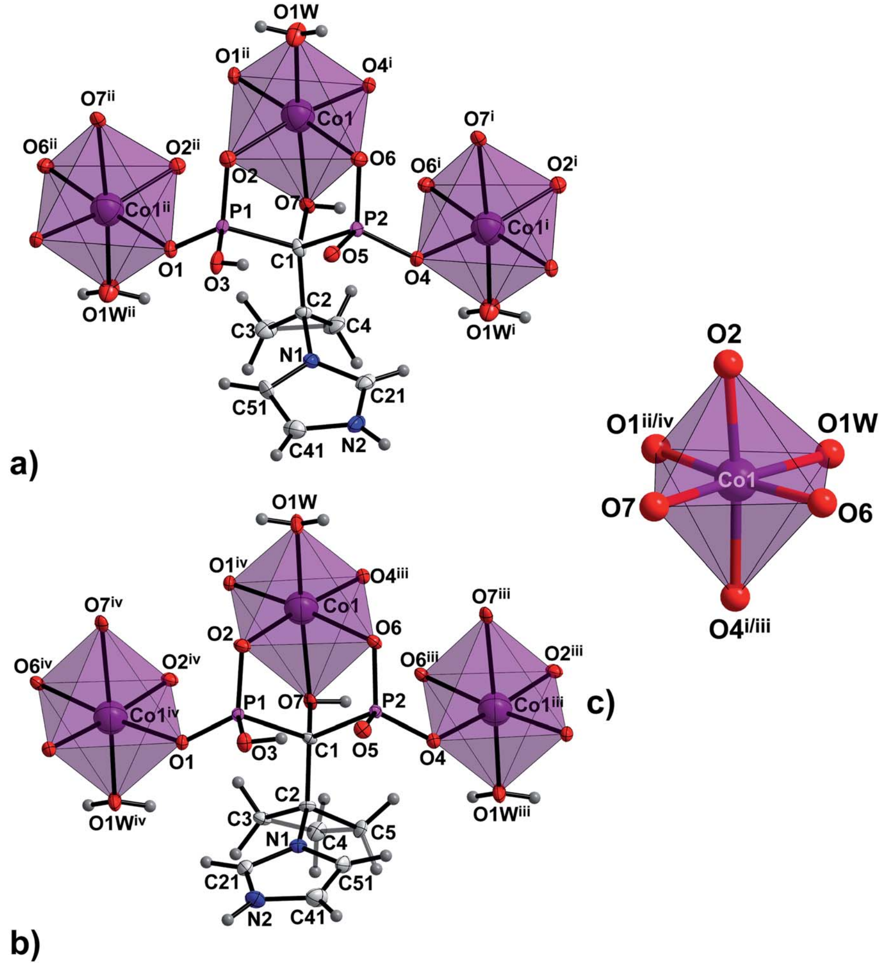

Fig. 1 The building unit and the atom-numbering scheme of (a) the representative compound **1a** and (b) **2a**. Lattice water molecules are omitted for clarity. Displacement ellipsoids for non-H atoms (except Co1) are drawn at 80% probability level. (c) Coordination environments of Co1 centre in **1a** and **2a**. Symmetry codes are given in Table S3 (ESI†).

twelve-membered rings into polymeric ladder-type structure (Fig. S11, ESI†).

3.3 IR characterization of 1a, 1b and 2a

The FT-IR spectra of the compounds **1a**, **1b** and **2a** are presented in Fig. S12–S15 (ESI†). The bands assignment (Table S5, ESI†) is based on detailed analysis of the IR spectra of H_4dmtZol, H_4cppZol, H_4cbtZol, H_4cptZol ligands supported by DFT calculations (ref. 31, Fig. S16, S17 and Table S6, ESI†) and tentative assignments for Co(II)/Ni(II) coordination polymers reported previously.[12–14]

The spectra of **1a**, **1b** and **2a** exhibit many common features manifested in location and intensity of characteristic bands assigned to ligand skeleton and functional groups. Additionally, the range 3600–3200 cm^{-1} is dominated by broad features associated with ν(O–H), ν(PO–H) and ν(N–H) stretching vibrations, consistent with presence of extensive hydrogen bonding involving water molecules (coordinated and lattice), phosphonate and imidazole groups (Table S4, ESI†). A week sharp band at *ca.* 3150 cm^{-1} is contributed by ν(C–H) vibrations of imidazole ring. The symmetric and asymmetric C–H stretching vibrations of cyclopropane/cyclobutane CH_2 groups give rise to a set of weak bands in the range 3050–2950 cm^{-1}. The band at *ca.* 1650 cm^{-1} corresponds to H–O–H bending vibrations of coordinated and lattice water molecules. The stretching vibrations of imidazole C=C, N=C and N–C bonds contribute weak bands observed at *ca.* 1580 and 1530 cm^{-1}. The region gathering most of the bending vibrations attributed to imidazole, cyclopropane/cyclobutane rings as well as hydroxyl C–O–H is located between *ca.* 1500 and 1150 cm^{-1}. Herein, noticeable differences in the spectra are associated with specific deformation vibrations of C_α substituents.

The phosphonate groups stretching and bending vibrations absorb mainly below 1350 cm^{-1}. Their detailed analysis supported by DFT calculations (see ref. 31 and Table S6, ESI†) have indicated that ν(P–O) vibrations are usually strongly mixed with δ(P–O–H) and stretching/deformation vibrations of imidazole ring and aliphatic substituents, thus making unambiguous interpretation of experimental IR spectra difficult. The bands near 1350 cm^{-1} are attributed to δ(P–O–H) vibrations. The ν(P–O) modes of P2 pendant O atom give rise to bands at *ca.* 1120 and 1030 cm^{-1}. The bands at *ca.* 945 and 840 cm^{-1} can be

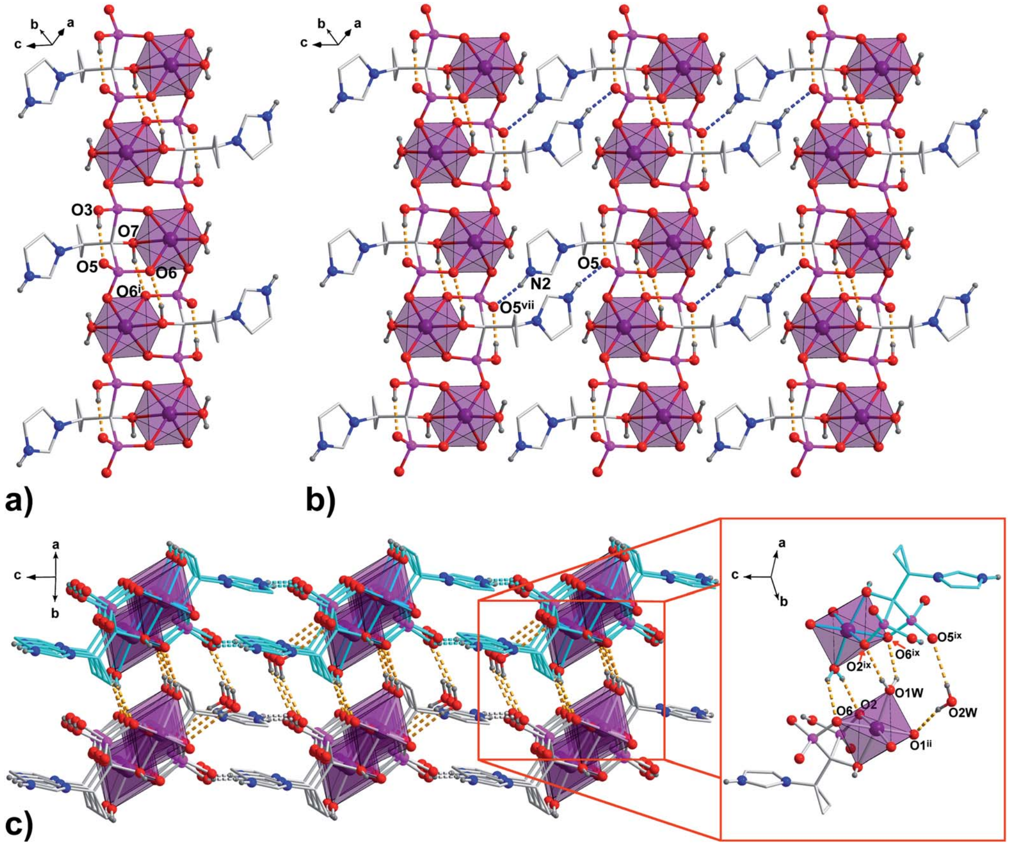

Fig. 2 The packing diagram of the representative **1a**. (a) 1D polymeric chain running along [110] crystallographic direction; (b) chains organized into 2D layer by N–H⋯O hydrogen bonds are shown as blue dashed lines; (c) 3D supramolecular network formed through connection of adjacent layers by O–H⋯O hydrogen bonds (orange dashed lines) between coordinated and lattice water molecules and phosphonate O-atoms. All H atoms not involved in the creation of hydrogen bonds and lattice water molecules (pictures a and b) are omitted for clarity. Symmetry codes are given in Table S4 (ESI†).

considered as contributed by ν(P–O) vibrations involving Co(II)/Ni(II)-coordinated phosphonate O atoms. The ν(P–OH) vibrations of P1 group contribute bands at lower 790–770 cm^{-1} wavenumbers. The vibrations contributed mostly by stretching of the C–P bond also appear below 800 cm^{-1}. The δ(O–P–O) deformation vibrations of phosphonate groups are observed around 500 cm^{-1}.

3.4 Thermal stabilities of 1a, 1b and 2a

Thermal decomposition of **1a**, **1b** and **2a** was investigated on crystalline samples by means of TG-DTA and DSC experiments conducted from room temperature up to 1000/600 °C under nitrogen and air atmosphere, respectively. Fig. 3 compiles TG curves in the temperature range 30–600 °C. Full set of experimental data is collected in Fig. S18–S23 (ESI†).

The studied compounds exhibit similar decomposition pathways with thermal stabilities decreasing in the order **1b** > **1a** > **2a**. The first step, taking place in the temperature ranges 236–271 °C (**1b**), 190–218 °C (**1a**) and 121–169 °C (**2a**), corresponds to release of lattice water molecule accompanied by weight loss of 4.62, 4.54, 5.18% (calcd 4.60, 4.61, 4.45%) with dehydration enthalpies ($\Delta H^{\circ}_{\mathrm{m}}$) of 9.98, 9.12, and 30.7 kJ mol^{-1}, respectively. The IR spectra of samples heated up to temperatures at which this process is completed clearly indicate that removal of lattice water has no negative impact on polymeric chains architecture (Fig. S24–S26, ESI†). On further heating up to 600 °C, compounds **1a** and **2a** behave similarly losing a total 24.4 and 27.9% weight in three distinct exothermic stages with maximum rates of reaction (T_{max}) of 303, 367, 430 (**1a**) and 257, 436, 508 °C (**2a**). For **1b**, only two exothermic processes accompanied by a total weight loss of 15.5% with T_{max} of 340 and 470 °C occur. These processes correspond to collapse of coordination chains by breaking M–O bonds, initiated by release of coordinated water molecule, then followed by elimination of C$_{\alpha}$-substituents and subsequent release of imidazole rings (Fig. S27–S29, ESI†). However, the IR spectrum shows that in **1b** the last process is not completed even at 600 °C (Fig. S30, ESI†).

The last stage of thermal decomposition starts above *ca.* 700 °C and is characterized by intense 31.5% (**1a**), 37.7% (**1b**) and 30.3% (**2a**) weight losses that can be attributed to combustion of organic parts of ligands. The resultant decomposition products constitute 39.5, 41.1 and 36.7% of initial samples masses and contain likely $Co_2(P_2O_7)$ (**1a**, **2a**) or $Ni_2(P_2O_7)$ (**1b**) (Fig. S31, ESI†). It is to note, that in contrast to previously analysed $Co_3(HL)_2(H_2O)_6\cdot 6H_2O$[12,13] and

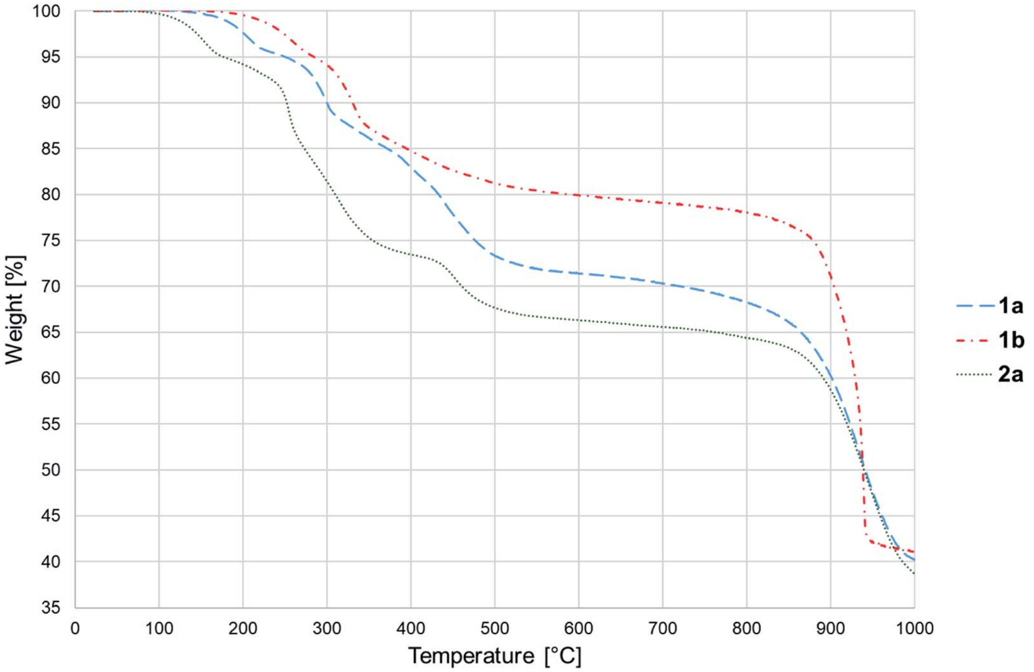

Fig. 3 TG curves recorded for **1a**, **1b** and **2a**.

$Co_3(HL)_2(H_2O)_4 \cdot 2H_2O$,[13] the products of **1a** and **2a** thermolysis are almost free from other residues (calcd 37.3, 36.03%). A support for such conclusion is provided by IR spectra revealing the absence of a weak band at *ca.* 1300 cm^{-1} (Fig. S32 and S33, ESI†).

3.5 NIR-UV/Vis spectroscopic characterization of 1a, 1b and 2a

In all **1a**, **1b** and **2a** the donor oxygen atoms form the $\{MO_4O'_2\}$ chromophore (M = Co(II)/Ni(II)) of pseudo-octahedral geometry compressed along the O4–M–O2 bond (Fig. 1 and S6, ESI†). It is to note, that the magnitude of compression increases with the increase of C_α substituent size ($T = 1.03$, 1.02 for **1a** and **1b**, $T = 1.05$ for **2a**).

In the solid-state diffuse-reflectance electronic spectra of **1a** and **2a** (Fig. 4), the absorption in the 5000 cm^{-1} to 30 000 cm^{-1} spectral range is attributed to the d–d transitions being characteristic for high-spin Co(II) ion (d^7 configuration). The spectra are almost identical with a lot of slightly marked maxima of the broad absorption in the 18 000–22 000 cm^{-1} range, thus confirming that crystal-field symmetry is lower than O_h. Consistent with the increase of tetragonal compression of the $\{MO_4O'_2\}$ octahedron (**2a** > **1a**), the maxima are better resolved in the spectrum of **2a**.

In the compressed tetragonal crystal field of D_4 symmetry, degenerate $^4T_{1g}(^4F, O_h)$ level splits into $^4A_2$ + ^4E components where the $^4A_2$ is the ground state.[33–35] The next quartet $^4T_{2g}((^4F), O_h)$ level consists of $^4E + {}^4B_2$ states, while the $^4A_{2g}(^4F, O_h)$ state is nondegenerate and transforms as $^4B_1$.[34,36] Likewise, the crystal field of D_4 symmetry causes splitting of the last quartet $^4T_{1g}((^4P), O_h)$ level into ^4E and $^4A_2$ states. As the absorption in 13 500–25 000 cm^{-1} spectral range is composed of multiple unresolved bands (Fig. 4), the spectra were deconvoluted with the use of variable digital filtering method[29] in order to refine band splitting and obtain energies of its components (Fig. S34, ESI†). The obtained pairs of bands with maxima at 6830 cm^{-1}, 8250 cm^{-1} (**1a**) and 6950 cm^{-1}, 8050 cm^{-1} (**2a**) are generated by spin-allowed quartet–quartet $^4A_2 \rightarrow 4E$ and $^4A_2 \rightarrow {}^4B_2$ transitions (^4E and $^4B_2$ states from $^4T_{2g}(^4F)$ in O_h).[37] However, the energy values 6830 cm^{-1} (**1a**) and 6950 cm^{-1} (**2a**) obtained for the $^4A_2 \rightarrow {}^4E$ transition are quite ambiguous because of presence of strong ligand bands in the region up to 7000 cm^{-1}. The spin and symmetry forbidden transitions become possible by splitting of the $^2E_g(^2G, O_h)$ state into $^2A_1$ + $^2B_1$. Under filtration process the pairs of bands at 10 210 cm^{-1}/12 510 cm^{-1} (**1a**) and 10 330 cm^{-1}/12 430 cm^{-1} (**2a**) clearly appeared and can be assigned to the $^4A_2 \rightarrow {}^2A_1$ and $^4A_2 \rightarrow {}^2B_1$ transitions, respectively. The well seen bands found at 14 010 cm^{-1} (**1a**) and 13 890 cm^{-1} (**2a**) originate from the spin-allowed quartet–quartet $^4A_2 \rightarrow {}^4B_1$ transition and are less intense as compared to other spin-allowed transitions. This assignment is drawn based on Wildner research explaining appearance of bands at 13 350 cm^{-1} and 15 200 cm^{-1} in the polarized (β polarization) electronic spectra of tetragonally distorted Co^{2+} octahedrons in $NaCo_2(SeO_3)_2OH$[37] and kieserite-type $CoSO_4 \cdot H_2O$ and $CoSeO_4 \cdot H_2O$ salts.[38] The same approach has also been applied to explain the origin of similar bands in the electronic spectrum of $[Co_3(HcptZol)_2(H_2O)_4] \cdot 2H_2O$.[13]

From the ^2G term, the $^2T_{1g}(^2G)$ and $^2T_{2g}(^2G)$ states split into pairs of $^2A_2$ + ^2E and $^2B_2$ + ^2E levels. The energies of these transitions are rather close to energy of quartet $^4B_1$ state, although they are situated between the bands correlated with quartet–quartet $^4A_2 \rightarrow {}^4B_1(^4F)$ and $^4A_2 \rightarrow {}^4E(^4P)$ transitions. In

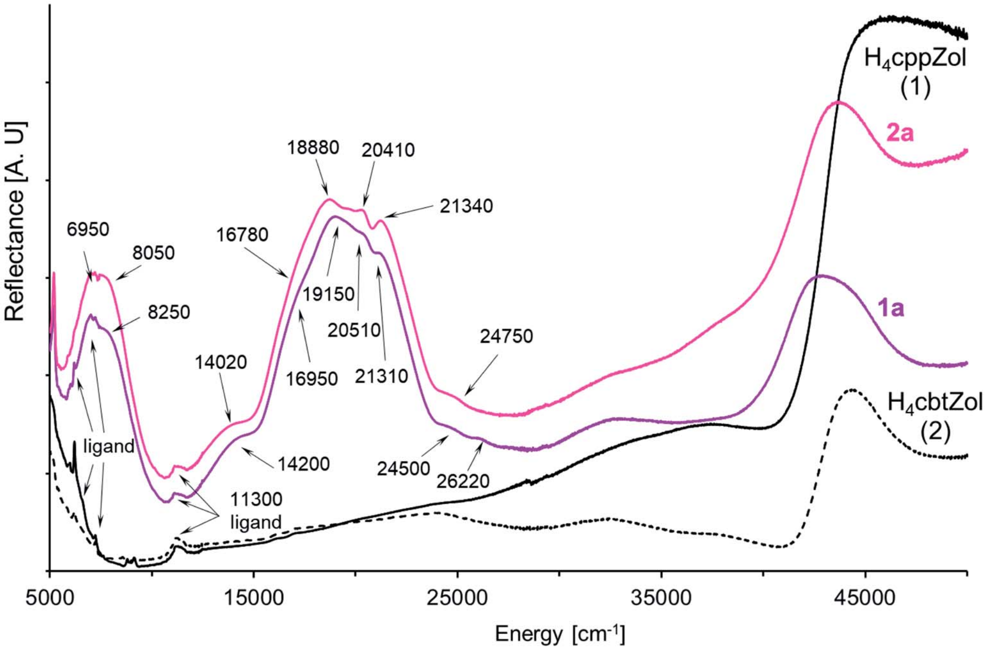

Fig. 4 The NIR-Vis-UV diffuse-reflectance electronic spectra of **1a**, **2a** and H_4cppZol, H_4cbtZol ligands (Scheme 1) obtained at room temperature.

the spectrum of **1a**, one band arises at 16 930 cm^{-1}, while for **2a** analogous band is splitting into two components with positions at 16 330 cm^{-1} and 17 170 cm^{-1} (Table 2, Fig. 4 and S34, ESI†).

The successive, well seen bands with maxima at 18850cm^{-1} (**1a**) and 18 650 cm^{-1} (**2a**) are correlated with spin-allowed transition to ^{4}E state being one of the two components of parental

Table 2 Band assignments, experimental and theoretical energies (cm^{-1}) of components of spin-allowed and spin-forbidden d–d transitions for **1a**, **1b** and **2a**^{a}

Cobalt(II) complexes (d^7 configuration)								Nickel(II) complex (d^8 configuration)				
Assignment	**1a**				**2a**			Assignment	**1b**			
O_h	D_4	Spect.	Filter	Calcd	Spect.	Filter	Calcd	O_h	D_4	Spect.	Filter	Calcd.
$^{4}T_{1g}(^{4}F)$	$^{4}A_2$	0	—	0	0	—	0	**$^{3}A_{2g}(^{3}F)$**	**$^{3}B_1$**	—	—	0
	^{4}E		—	2001	—	—	1966					
$^{4}T_{2g}(^{4}F)$	**^{4}E**	**6830**	**6830**	**6734**	**6950**	**6950**	**6629**	**$^{3}T_{2g}(^{3}F)$**	**$^{3}B_2$**	**7000**	**6990**	**6590**
	$4B_2$	**8250**	**8250**	**8226**	**8050**	**8050**	**8190**		**$^{3}E(1)$**	**8500**	**8370**	**8310**
$^{2}E_g(^{2}G)$	$2A_1$	—	10 210	11 309	—	10 330	11 275					
Ligand		11 300	11 350	—	11 300	11 330	—	Ligand		11 230	11 430	—
	$^{2}B_1$	—	12 510	12 444	—	12 430	12 266	**$^{3}T_{1g}(^{3}F)$**	**$^{3}A_2$**	13 040	**12 890**	**12 860**
$^{4}A_{2g}(^{4}F)$	**$^{4}B_1$**	**14 200**	**14 010**	**14 059**	**14 020**	**13 890**	**13 908**		**$^{3}E(2)$**	13 040	**12 890**	**12 955**
$^{2}T_{1g}(^{2}G)$	$^{2}A_2$	—	—	15 539	—		15 419					
$^{2}T_{2g}(^{2}G)$	$^{2}B_2$	16 950	16 930	16 852	16 780	16 330	16 623	$^{1}E_g$ (^{1}D)	$^{1}A_1$	14 660	14 770	14 470
$^{2}T_{2g}(^{2}G)$	^{2}E	—	—	17 440	—	17 170	17 326		$^{1}B_1$	14 660	14 770	14 570
$^{2}T_{1g}(^{2}G)$	^{2}E	—	—	17 924	—		17 743	$^{1}A_{1g}(^{1}G)$	1	20 600	20 490	20 860
$^{4}T_{1g}(^{4}P)$	**^{4}E**	**19 150**	**18 850**	**18 685**	**18 880**	**18 650**	**18 620**	$^{1}T_{2g}(^{1}D)$	$^{1}B_2$	—	—	22 250
$^{2}T_{1g}(^{2}P)$	$^{2}A_2$	20 510	20 310	20 461	20 410	20 350	20 310		^{1}E	23 100	23 190	23 250
$^{2}A_{1g}(^{2}G)$	$^{2}A_1$	—	—	21 280			21 048					
$^{4}T_{1g}(^{4}P)$	**$^{4}A_2$**	**21 310**	**21 650**	**21 741**	**21 340**	**21 490**	**21 520**	**$^{3}T_{1g}(^{3}P)$**	**$^{3}A_2$**	**24 200**	**24 290**	**24 230**
$^{2}T_{1g}(^{2}P)$	$^{2}E_2$	—	—	21 760	—	—	21 616		**$^{3}E(3)$**	**24 200**	**24 290**	**24 320**
$^{2}T_{2g}(^{2}G)$	^{2}E	—	—	24 189	—	—	24 562					
$^{2}T_{1g}(^{2}G)$	^{2}E	24 500	24 830	24 811	24 750	24 810	24 710	$^{1}T_{1g}(^{1}G)$	$^{1}A_2$	—	25 170	25 215
$^{2}T_{2g}(^{2}G)$	$^{2}B_2$	—	—	24 902	—	—	26 035		^{1}E	—	—	27 310
$^{2}T_{1g}(^{2}G)$	$^{2}A_2$	26 220	26 270	26 226	—	26 370	26 331					

[a] Spect. – the energy found form the experimental spectra; filter – the energy found from the filtering process (filter parameters: (**1a**) step = 20 cm^{-1}, $\alpha = 400$ and $N = 40$; (**2a**) step = 20 cm^{-1}, $\alpha = 400$ and $N = 30$; (**1b**) step = 20 cm^{-1}, $\alpha = 300$ and $N = 30$); calcd – calculated energy; – not observed; the spin-allowed transitions are marked in bold.

$^4T_{1g}((^4P), O_h)$ level. The second component, $^4A_2(^4T_{1g}, ^4P)$ state, is expected higher. The energies of $^4A_2 \rightarrow {}^4E$ and $^4A_2 \rightarrow {}^4A_2(^4P)$ transitions correspond to 18 850 cm^{-1}/21 650 cm^{-1} for **1a** and 18 650 cm^{-1}/21 490 cm^{-1} for **2a** (Table 2, Fig. S34, ESI†). Indeed, a detailed filtration analysis of 19 000–21 000 cm^{-1} region has revealed the presence of extra bands between these pairs of bands, which can be correlated with the combined spin- and symmetry forbidden transitions. The $^2T_{1g}(^2P)$ state involves the $^2A_2$ and ^2E levels, while the $^2A_{1g}$ state from the ^2G term is nondegenerate and keeps its symbol ($^2A_1$). We tentatively assigned the energy of $^4A_2 \rightarrow {}^2A_2(^2T_{1g}, ^2P)$ transition as 20 310 cm^{-1} for **1a** and 20 350 cm^{-1} for **2a**. Neither corresponding band has been found in the spectra for the $^4A_2 \rightarrow {}^2A_1(^2A_{1g}, ^2G)$ or $^4A_2 \rightarrow {}^2E(^2T_{1g}, ^2P)$ transitions (Fig. S34, ESI†).

Further, in the region between 22 000 cm^{-1} and the charge transfer absorption edge, a weak spectral feature at 30 000 cm^{-1} is present (Fig. 4) that can only be attributed to the spin-forbidden transitions. An assignment of feature attributed to the components of remaining spin-forbidden $^4A_2 \rightarrow {}^2E + {}^2B_2(^2T_{2g}, ^2G, O_h)$ and $^4A_2 \rightarrow {}^2E + {}^2A_2(^2T_{1g}, ^2G, O_h)$ transitions is ambiguous. Finally, weak bands observed at 24 830 cm^{-1}/26 270 cm^{-1} in the spectrum of **1a** and at 24 810 cm^{-1}/26 370 cm^{-1} in the spectrum of **2a** are caused by spin-forbidden transitions from the ground state to higher doublet $^2T_{1g}(^2G, O_h)$ state.

The diffuse-reflectance spectrum of **1b** shows three main regions of absorption: 5800–10 000 cm^{-1}, 10 500–17 000 cm^{-1} and 18 800–28 700 cm^{-1}, which are characteristic for the three spin-allowed: I-st ($^3A_{2g} \rightarrow {}^3T_{2g}(^3F, O_h)$), II-nd ($^3A_{2g} \rightarrow {}^3T_{1g}(^3F, O_h)$) and III-rd ($^3A_{2g} \rightarrow {}^3T_{1g}(^3P, O_h)$) d–d transitions for nickel(II) ion of d^8 configuration in a pseudooctahedral crystal field (Fig. 5). These broad bands are slightly asymmetric and exhibit pairs of maxima at *ca.* 7000 cm^{-1} and 8500 cm^{-1} (I-st d–d), 11 230 cm^{-1} and 13 040 cm^{-1} (II-nd d–d) as well as 20 600 cm^{-1} and 24 200 cm^{-1} (III-rd d–d). Moreover, the spectrum presents sharp feature at 14 660 cm^{-1} as well as a shoulder on the low energetic branch of III-r d d–d at *ca.* 20 600 cm^{-1}.

Generally, the bands corresponding to d–d transitions are red-shifted with respect to related bands in the spectrum of recently reported $[Ni_3(HdmtZol)_2(H_2O)_6]\cdot 6H_2O$.[14] This indicates that energies of d–d transitions are lower. Indeed, smaller tetragonal compression around Ni(II) ($T = 1.02$) leads to noticeably lower asymmetry of d–d bands compared with those recorded for Ni(II) complex based on HdmtZol^{3-} ligand ($T = 1.04$).

The filtering process has revealed splitting of I-st and III-rd d–d bands into two components (Fig. S35, ESI†), which justifies an analysis based on the model assuming slightly compressed tetragonal D_4 symmetry with $^3B_1$ state as a ground term.[33,39] The tetragonal crystal filed causes splitting of each spin allowed d–d band as follows: $^3T_{2g}(^3F, O_h)$ state splits into $^3B_2$ and $^3E(1)$, $^3T_{1g}(^3F, O_h)$ splits into $^3E(2) + {}^3A_2$ states and third state $^3T_{1g}(^3P, O_h)$ consists of $^3E(3)$ and $^3A_2$ levels. According to the energy level diagram,[33,39] the spin and symmetry–forbidden transitions also become possible by splitting of the ^1E_g and $^1T_{2g}$ states (both from ^1D term, O_h) into $^1B_1 + {}^1A_1$ and $^1B_2 + {}^1E$ levels, respectively. The $^1A_{1g}$ state from ^1G term is nondegenerate and stays the same ($^1A_1$), while successive $^1T_{1g}$ state from the ^1G term consists of ^1E and $^1A_2$ levels.

The $^3B_1 \rightarrow {}^3B_2$ and $^3B_1 \rightarrow {}^3E(1)$ transitions with energies found under filtration process to be *ca.* 6990 cm^{-1} and 8370 cm^{-1} are assigned as components of the I-st d–d band. These experimental energies stay in good agreement with the calculated ones (Table 2). The calculated energies obtained for $^3B_1 \rightarrow {}^3A_2$ and $^3B_1 \rightarrow {}^3E(2)$ transitions (II-nd d–d) equal 12 860 and 12 955 cm^{-1}. However, due to a very small difference in energy values of *ca.* ∼100 cm^{-1}, even the filter does not revel splitting but only a shoulder effect. The sharp feature at 14 770 cm^{-1} arises from ^1E_g in O_h and is composed of $^1A_1 + {}^1B_1$ in D_4. The splitting of this band corresponding to spin-forbidden transition is very difficult to observe in diffuse-reflectance spectrum, however, is confirmed by calculations giving the values of energies of 14 470 cm^{-1} and 14 570 cm^{-1} for $^1A_1$ and $^1B_1$ states, respectively. The experimental energy of subsequent spin-forbidden transition, $^3B_1 \rightarrow {}^1A_1(^1A_{1g}, ^1G)$ at 20 490 cm^{-1}, corresponds well with calculated value of 20 860 cm^{-1}. The $^3B_1 \rightarrow {}^1B_2 + {}^1E$ transitions, being the components of $^1T_{2g}(^1D, O_h)$ state, are usually situated between the II-nd and III-rd d–d bands. A single band is found in filtering process at 23 190 cm^{-1} with low energetic shoulder at 22 230 cm^{-1}, while calculated energies of these states are 22 250 cm^{-1} and 23 250 cm^{-1}. The III-rd d–d band observed with maximum at 24 290 cm^{-1} seems to remain unsplitted. Its position is confirmed by close values of calculated energies of 24 230 cm^{-1} and 24 320 cm^{-1} obtained for $^3B_1 \rightarrow {}^3A_2$ and $^3B_1 \rightarrow {}^3E(3)$ transitions. Finally, the bands of higher energetic transitions of forbidden nature, namely, $^3B_1 \rightarrow {}^1A_2(^1T_{1g}(G), O_h)$ and $^3B_1 \rightarrow {}^1E(^1T_{1g}(G), O_h)$ are expected over 25 000 cm^{-1}. Their energies were calculated as 25 215 cm^{-1} and 27 310 cm^{-1}, however, they are not observed in the spectrum even as an effect of filtration (Fig. S35, ESI†).

The observed and calculated energy levels alongside with corresponding assignments are collected in Table 2. The agreement between the observed and calculated values is relatively satisfying. For cobalt(II) compounds (**1a** and **2a**), the tetragonal crystal field parameters D_q, D_t and D_s as well as the Racah parameters B and C were calculated using the energies of quartet–quartet transitions. The following sets were obtained: $D_q = 583$ cm^{-1}, $D_t = -168$ cm^{-1}, $D_s = 568$ cm^{-1}, $B = 890$ cm^{-1}, $C/B = 4.12$ (**1a**) and $D_q = 572$ cm^{-1}, $D_t = -177$ cm^{-1}, $D_s = 537$ cm^{-1}, $B = 888$ cm^{-1}, $C/B = 4.08$ (**2a**). The Dt is dependent on the splitting of the first quartet state of the octahedral $^4T_{2g}(^4F)$ and its negative sing calculated for both **1a** and **2a** is in agreement with the compressed geometry of $\{CoO_6\}$ polyhedrons in $NaCo_2(SeO_3)(OH)$[37] and $[Co_3(HcptZol)_2(H2O)_4]$ coordination unit.[13] For nickel(II) complex **1b**, the values of D_q, D_s, D_t and Racah parameter B were calculated using the energies of six-triplet states. The following values were obtained: $D_q = 659$ cm^{-1} (exp. energy 699 cm^{-1} for $^3B_1 \rightarrow {}^3B_2$ transition, Table 2), $D_s = 307$ cm^{-1}, $D_t = -196$ cm^{-1} and $B = 932$ cm^{-1}.

3.6 Magnetic properties of 1a, 1b and 2a

The magnetic susceptibilities of **1a**, **2a**, and **1b** show Curie–Weiss behaviour above *ca.* 50 K with the Weiss constants $\theta = -12.4$, -8.3, and -2.1 K, and magnetic moments of 5.32 (2.75),

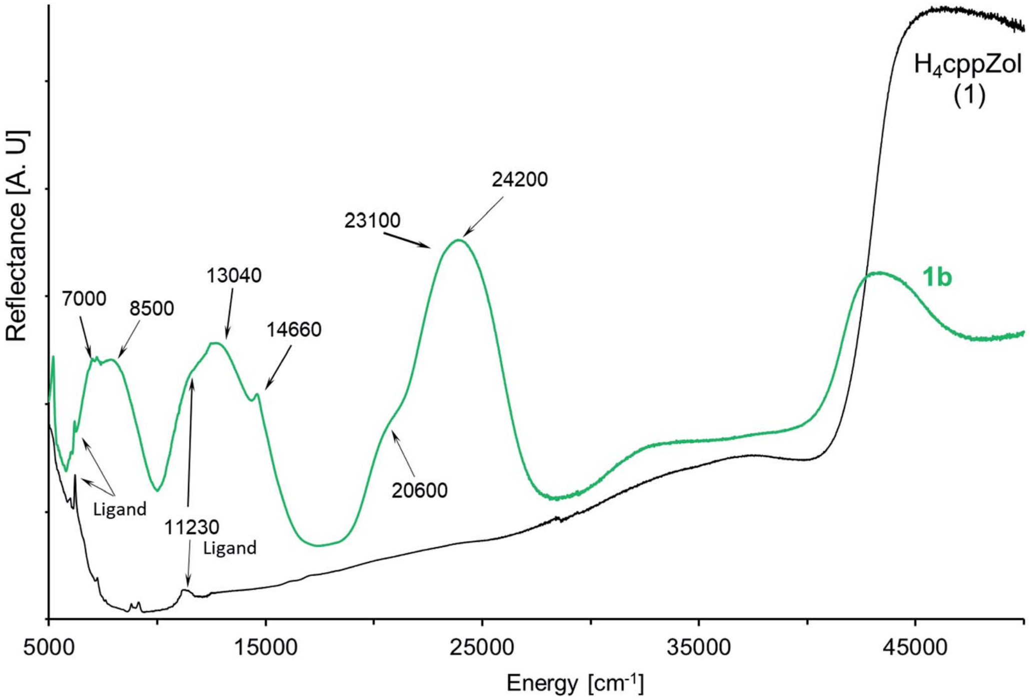

Fig. 5 The NIR-Vis-UV diffuse-reflectance electronic spectra of **1b** and related H$_4$cppZol ligand (Scheme 1) obtained at room temperature.

5.23 (2.70), and 3.34 (2.30) μ_B, respectively. The expected values for *g* factors corresponding to the respective moments for free Co(II) (**1a**, **2a**) or Ni(II) (**1b**) ions are given in brackets. Full results of magnetic measurements and calculations are presented in Fig. S36–S39 (ESI†). The magnetic behaviours of **1a** and **2a** are very similar, therefore Fig. 6 presents the temperature dependence of the effective magnetic moments (μ_{eff}) only for **1a** and **1b**. The magnetic susceptibilities of both compounds increase monotonically as the temperature is decreased up to 1.7 K. Upon cooling, the effective magnetic moment of Co(II) complex **1a** slightly decreases from 300 to 100 K and then decreases faster, reaching a value of 4.1 μ_B at ~2 K. An effective moment of the nickel complex **1b** slowly decreases below room temperature, reaches a shallow minimum at 55 K, then passes through a pronounced maximum at 5 K and drops sharply below this temperature.

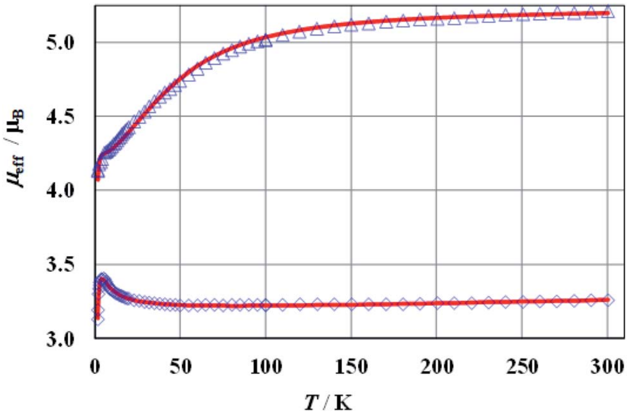

Fig. 6 Effective magnetic moment of **1a** at B = 100 mT (triangles) and **1b** at B = 500 mT (diamonds). The solid lines represent the theoretical fits (see the text).

The crystals structures of all the compounds comprise zig–zag chains, in which metal centres are alternately linked by double, symmetrical (–O1–P1–O2–)$_2$ and (–O4–P2–O6–)$_2$ bridges (Fig. S8†). Therefore, the magnetic susceptibility of **1a**, **2a** and **1b** was analyzed in the framework of an alternating-exchange spin-chain.

Using the Hamiltonian:

$$H = -J_1\sum S_{2i}S_{2i+1} - J_2\sum S_{2i+1}S_{2i+2} \tag{1}$$

Cortés[40] has derived the exact expression for magnetic susceptibility of J_1J_2 alternating chain with Heisenberg-type exchange between the classical spins:

$$\chi_{\text{alt}} = N\beta^2g^2S(S+1)/3k_BT\cdot F_{\text{alt}} \tag{2}$$

$$F_{\text{alt}} = (1 + u_1 + u_2 + u_1u_2)/(1 - u_1u_2) \tag{3}$$

where $u_i = \coth[J_iS(S+1)/k_BT] - k_BT/J_iS(S+1)$ and N, β, g, and k_B have their usual meanings.

If the antiferromagnetic coupling is weak or its character is ferromagnetic, the influence of zero-field splitting (zfs) must be taken into account in an analysis of the magnetic behaviour at low temperatures. The bulk susceptibility of **1a**, **2a** and **1b** was calculated in the full temperature range by the combination of zfs and the alternating chain[41–43] as:

$$\chi = \chi_{\text{zfs}}F_{\text{alt}} + \text{TIP}. \tag{4}$$

According to Boca,[44] the zfs contribution can be represented by $\chi_{zfs} = (\chi_{\parallel} + 2\chi_{\perp})/3$ where:

$$\chi_{\parallel} = (N\beta^2 g_{\parallel}^2/4k_BT)(1 + 9d^2) / (1 + d^2), \tag{5a}$$

$$\chi_{\perp} = (N\beta^2 g_{\perp}^2/k_BT)\,[1 + 3k_BT/4D\cdot(1 - d^2)]/(1 + d^2), \tag{5b}$$

for the cobalt compounds (**1a**, **2a**) or:

$$\chi_{\parallel} = (N\beta^2 g_{\parallel}^2/k_BT)2d/(1 + 2d), \tag{6a}$$

$$\chi_{\perp} = (N\beta^2 g_{\perp}^2/k_BT)2k_BT/D\cdot(1 - d)/(1 + 2d) \tag{6b}$$

for the nickel compound (**1b**), D is the axial zfs parameter and $d = e^{-D/k_BT}$. In order to avoid overparametrization, isotropic g values were assumed.

The best agreement between theory and experiment was obtained for $J_1 = -0.72$, -1.07, -2.47 cm^{-1}, $J_2 = 0.33$, 0.42, 0.67 cm^{-1}, $D = 58.2$, 51.4, -1.86 cm^{-1}, $g = 2.69$, 2.67, 2.25, and R (defined as $\Sigma[(\chi T)_{exp} - (\chi T)_{calc}]^2/\Sigma[(\chi T)_{exp}]^2$) equal to 6.2×10^{-5}, 5.6×10^{-5}, 7.8×10^{-6}, for **1a**, **2a** and **1b**, respectively. During the calculations, the temperature independent paramagnetism (TIP) was fixed at 60×10^{-6} emu per Co. Good fit of calculated and experimental values of magnetic susceptibility of **1b** at temperatures above 100 K could be achieved with a TIP value of 201×10^{-6} emu per Ni. The susceptibility curves resulting from the above parameters (depicted as $\mu_{eff}(T)$ and $\chi^{-1}(T)$) are shown in Fig. 6 and S36–S38 (ESI†). Since it is not possible to calculate field dependent magnetization within the above model, we have tried to ignore weak exchange interactions, treating the system as a set of isolated Co(II) ions and leaving the rest of the parameters unchanged. The $M(B)$ dependences calculated for various external fields are drawn in Fig. S39 (ESI†) as a solid line and fit the experimental data pretty well.

The magnetic susceptibility of cobalt compounds calculated in the zero magnetic field using formulas 2–5 does not depend on the sign of the D parameter. In strong magnetic fields (above ~0.5 T) a significant difference between the magnetization calculated for D and $-D$ is observed (Fig. S39, ESI†) with a clear indication of positive values. This corresponds to the compressed tetragonal bipyramid around the cobalt centres (Fig. 1) and is consistent with the results of the analysis of the electronic spectra of **1a** and **2a**. It is also possible to fit the temperature dependence of magnetic susceptibility using both positive and negative values of parameter D for the nickel compound (**1b**). However, in this case the set of selected parameters with negative D (which again corresponds to the compressed bipyramid) better describes the behaviour of magnetization as a function of the magnetic field (Fig S39, ESI†).

Although coordination compounds containing various metal centres connected by –O–P–O– bridges are quite common and the magnetic properties of many of them have been investigated,[15b,17b,18,20,22,45–49] a question still arises about the nature of magnetic exchange couplings through –O–P–O– bridges. Correlations of exchange integrals with M–O–P–O dihedral angles (related to deviation of the phosphonate group from the mean M–O···O–M plane)[45,46] or with the angle between the O–P–O plane and the M–O axis,[47] supported by the DFT calculations,[46,48a] suggest that the most important structural parameter controlling the exchange coupling is the M–O···O–M dihedral angle over the O–P–O bridge. The antiferromagnetic coupling decreases with the increase of the M–O···O–M angle and the coupling can become ferromagnetic in the case of larger angles.[46,48,49] The J values calculated for **1a**, **2a** and **2b** can readily be rationalized in terms of magnetostructural correlations outlined above. For both **1a** and **2a**, the boundary between ferro- and antiferromagnetic couplings estimated by this method for Co–O···O–Co angle is *ca.* 80°, and as seen in Fig. S40 and Table S7 (ESI†), the same observation seems to be applicable for 1D $Co_3(HL)_2(H_2O)_6\cdot 6H_2O$ polymers featuring chains of linear symmetric Co2 Co1 Co2 trimers (HL = HdmtZol^{3-}, HcppZol^{3-}, HcbtZol^{3-}, Scheme 1).[12,13] Moreover, the same value can also be used to explain magnetic behaviour of **1b** and recently reported $Ni_3(HdmtZol)_2(H_2O)_6\cdot 6H_2O$ complex.[14]

4. Conclusions

Three Co(II) and Ni(II) 1D coordination polymers based on zoledronic acid analogues with a cyclopropane (cpp) or cyclobutane (cbt) ring on the C_α carbon, namely $[Co(H_2cppZol)(H_2O)]\cdot H_2O$ (**1a**), $[Ni(H_2cppZol)(H_2O)]\cdot H_2O$ (**1b**) and $[Co(H_2cbtZol)(H_2O)]\cdot H_2O$ (**2a**), were synthesized under hydrothermal conditions and characterized by means of single-crystal X-ray diffraction, spectroscopic and thermal techniques. The studied compounds exhibit 1D double zig–zag chains architecture with the 8 + 8 rings motif formed by alternately arranged symmetrical $(-O-P-O-)_2$ bridges linking equivalent octahedral Co(II)/Ni(II) centres.

All the compounds exhibit similar decomposition pathways upon heating with thermal stabilities decreasing in the order **1b** > **1a** > **2a**. The IR spectra revealed that lattice water release does not change chains architecture leaving them intact up to *ca.* 320, 280 and 240 °C, respectively. A good correlation between calculated energies of d–d transitions and experimental NIR-UV/VIS spectra was obtained with the assumption that metal centres of **1a**, **1b** and **2a** adopt pseudo-octahedral compressed geometry.

Variable temperature magnetic susceptibility measurements analyzed in the framework of an alternating-exchange spin-chain revealed the occurrence of weak alternating antiferromagnetic–ferromagnetic exchange interactions propagated between the magnetic centres along double $(-O-P-O-)_2$ bridges with $J_1 = -0.72$, -1.07, -2.47 cm^{-1} and $J_2 = 0.33$, 0.42, 0.67 cm^{-1} for **1a**, **1b** and **2a** respectively. The boundary between antiferro- and ferromagnetic couplings for Co–O···O–Co angle was established to be *ca.* 80°. This value can also be used to explain magnetic behaviour of **1b** and is applicable for recently reported $M_3(HL)_2(H_2O)_6\cdot 6H_2O$ (M = Co, Ni) complexes based on α,α-disubstituted analogues of zoledronic acid.

Conflicts of interest

There are no conflicts to declare.

Acknowledgements

Financial support by a statutory activity subsidy from the Polish Ministry of Science and Higher Education for the Department of Chemistry of Wroclaw University of Science and Technology is gratefully acknowledged.

References

1 J. Goura and V. Chandrasekhar, *Chem. Rev.*, 2015, **115**, 6854.

2 (*a*) P. Bhanja and A. Bhaumik, *ChemCatChem*, 2016, **8**, 1607; (*b*) C.-Y. Gao, J. Ai, H.-R. Tian, D. Wu and Z.-M. Sun, *Chem. Commun.*, 2017, **53**, 1293; (*c*) Y.-P. Zhu, T.-Z. Ren and Z.-Y. Yuan, *Catal. Sci. Technol.*, 2015, **5**, 4258.

3 K. J. Gagnon, H. P. Perry and A. Clearfield, *Chem. Rev.*, 2012, **112**, 1034.

4 (*a*) S. M. Lane, J. Monot, M. Petit, B. Bujoli and D. R. Talham, *Colloids Surf., B*, 2007, **58**, 34; (*b*) B. Bujoli, P. Janvier and M. Petit, in *Metal Phosphonate Chemistry: From Synthesis to Applications*, ed. A. Clearfield and K. Demadis, Royal Society of Chemistry, Cambridge, 2012, vol. 13, p. 420.

5 G. B. Hix, in *Metal Phosphonate Chemistry: From Synthesis to Applications*, ed. A. Clearfield and K. Demadis, Royal Society of Chemistry, Cambridge, 2012, vol. 16 p. 525.

6 (*a*) H. Xu, H. Zhou, L. Feng, Q. Wang, R. Chen, W. Huang and X. Wu, *Dalton Trans.*, 2018, **47**, 11226; (*b*) M. S. M. Abdelbaky, Z. Amghouz, D. Martínez Blanco, S. García-Granda and J. R. García, *J. Solid State Chem.*, 2017, **248**, 61; (*c*) S.-S. Bao and L.-M. Zheng, *Coord. Chem. Rev.*, 2016, **319**, 63.

7 E. Matczak-Jon and V. Videnova-Adrabińska, *Coord. Chem. Rev.*, 2005, **249**, 2458.

8 (*a*) D.-K. Cao, X.-J. Xie, Y.-Z. Li and L.-M. Zheng, *Dalton Trans.*, 2008, **0**, 5008; (*b*) X.-L. Zhang, K. Cheng, F. Wang and J. Zhang, *Dalton Trans.*, 2014, **43**, 285.

9 (*a*) F. H. Ebetino, A.-M. L. Hogan, S. Sun, M. K. Tsoumpra, X. Duan, J. T. Triffitt, A. A. Kwaasi, J. E. Dunford, B. L. Barnett, U. Oppermann, M. W. Lundy, A. Boyde, B. A. Kashemirov, C. E. McKenna and R. G. G. Russell, *Bone*, 2011, **49**, 20; (*b*) R. G. G. Russell, *Bone*, 2011, **49**, 2; (*c*) M. Mc Clung, S. T. Harris, P. D. Miller, D. C. Bauer, K. S. Davison, L. Dian, D. A. Hanley, D. L. Kendler, C. K. Yuen and E. M. Lewiecki, *Am. J. Med.*, 2013, **126**, 13; (*d*) S. E. Papapoulos, *Nat. Rev. Rheumatol.*, 2013, **9**, 263; (*e*) L. Michou and J. P. Brown, *Drug Des., Dev. Ther.*, 2011, **5**, 225; (*f*) H. Fleisch, *Bisphosphonates in bone disease: from the laboratory to the patient*, Academic Press, San Diego, 2000; (*g*) J. E. Brown and R. E Coleman, *Breast Cancer Res.*, 2002, **4**, 24; (*h*) S. Ahmad, G. Kuraganti and D. Steenkamp, *Am. J. Med.*, 2015, **128**, 239.

10 (*a*) Q.-J. Niu, Y.-Q. Zheng, H.-L. Zhu and W. Xu, *Transition Met. Chem.*, 2014, **41**, 365; (*b*) E. Freire, M. Quintero, D. Vega and R. Baggio, *Inorg. Chim. Acta*, 2013, **394**, 229; (*c*) Q.-J. Niu, Y.-Q. Zheng, L.-X. Zhou and H.-L. Zhu, *J. Solid State Chem.*, 2015, **227**, 212.

11 (*a*) W. Goldeman and T. Rojek, *PL Pat.* application, 408 018 A1, 2014; (*b*) W. Goldeman and T. Rojek, *PL Pat.* application, 408 029 A1, 2014.

12 T. Rojek, W. Goldeman, K. Ślepokura, M. Duczmal, A. Wojciechowska and E. Matczak-Jon, *Dalton Trans.*, 2017, **46**, 6900.

13 T. Rojek, W. Goldeman, K. Ślepokura, M. Duczmal, A. Wojciechowska and E. Matczak-Jon, *New J. Chem.*, 2018, **42**, 7830.

14 T. Rojek, W. Goldeman, K. Ślepokura, M. Duczmal, A. Wojciechowska and E. Matczak-Jon, *Polyhedron*, 2018, **141**, 44.

15 (*a*) D. K. Cao, Y. Z. Li and L. M. Zheng, *Inorg. Chem.*, 2007, **46**, 7571; (*b*) D. K. Cao, M. J. Liu, J. Huang, S. S. Bao and L. M. Zheng, *Inorg. Chem.*, 2011, **50**, 2278.

16 C. R. Groom, I. J. Bruno, M. P. Lightfoot and S. C. Ward, *Acta Crystallogr., Sect. B: Struct. Sci., Cryst. Eng. Mater.*, 2016, **72**, 171.

17 (*a*) W.-Y. Yin, W.-S. Cai, Y.-S. Ma, X.-Y. Tang and R.-X. Yuan, *J. Mol. Eng. Mater.*, 2014, **2**, 1440003; (*b*) Y.-S. Ma, W.-Y. Yin, W.-S. Cai, P.-Z. Zhu, X.-Y. Tang, R.-X. Yuan and S. Roy, *RSC Adv.*, 2013, **3**, 18430.

18 (*a*) Y. Ma, R. Yuan and L. Zheng, *Inorg. Chem. Commun.*, 2009, **12**, 860; (*b*) K.-R. Ma, L. Cao, M.-H. Cong, Y.-H. Kan and R.-Q. Li, *J. Mol. Struct.*, 2017, **1139**, 67.

19 (*a*) Y. Gong, W. Tang, W. Hou, Z. Zha and C. Hu, *Inorg. Chem.*, 2006, **45**, 4987; (*b*) G. Li, Y. Fan, T. Zhang, T. Ge and H. Hou, *J. Coord. Chem.*, 2008, **61**, 540.

20 Z.-C. Zhang, S.-S. Bao and L.-M. Zheng, *Inorg. Chem. Commun.*, 2007, **10**, 1063.

21 D.-K. Cao, M.-J. Liu, J. Huang, S.-S. Bao and L.-M. Zheng, *Inorg. Chem.*, 2011, **50**, 2278.

22 (*a*) K.-R. Ma, Y. Zhang, Y.-H. Kan, X.-J. Yang and M.-H. Cong, *Synth. Met.*, 2013, **182**, 40; (*b*) Z.-C. Zhang, S. Gao and L.-M. Zheng, *Dalton Trans.*, 2007, **0**, 4681; (*c*) J. Zhao, J. Wu, J. Hu, H. Hou and Y. Fan, *Inorg. Chim. Acta*, 2010, **363**, 662.

23 D. Liu, S. A. Kramer, R. C. Huxford-Phillips, S. Wang, J. Della Rocca and W. Lin, *Chem. Commun.*, 2012, **48**, 2668.

24 E. Alvarez, A. G. Marquez, T. Devic, N. Steunou, C. Serre, C. Bonhomme, C. Gervais, I. Izquierdo-Barba, M. Vallet-Regi, D. Laurencin, F. Maurif and P. Horcajada, *CrystEngComm*, 2013, **15**, 9899.

25 (*a*) CrysAlisPro, Agilent Technologies, Yarnton, U. K., 2012; (*b*) CrysAlisPro, Rigaku Oxford Diffraction, Yarnton, U. K., 2015, 2018.

26 G. M. Sheldrick, *Acta Crystallogr., Sect. A: Found. Crystallogr.*, 2008, **64**, 112.

27 G. M. Sheldrick, *Acta Crystallogr., Sect. C: Struct. Chem.*, 2015, **71**, 3.

28 K. Brandenburg and K. Putz, *DIAMOND, Ver. 3.2, Crystal and Molecular Structure Visualization*, University of Bonn, Germany, 2006.

29 (*a*) J. Myrczek, *Spectrosc. Lett.*, 1990, **23**, 1027; (*b*) A. Wojciechowska, Z. Staszak, W. Bronowska, A. Pietraszko and M. Cieślak-Golonka, *Polyhedron*, 2001, **20**, 2063; (*c*) A. Wojciechowska, A. Gągor, M. Duczmal, Z. Staszak and A. Ożarowski, *Inorg. Chem.*, 2013, **52**, 4360; (*d*) A. Wojciechowska, M. Daszkiewicz, Z. Staszak, A. Trusz-

Zdybek, A. Bieńko and A. Ożarowski, *Inorg. Chem.*, 2011, **50**, 11532.

30 B. Murphy, M. Aljabri, A. M. Ahmed, G. Murphy, B. J. Hathaway, M. E. Light, T. Geilbrich and M. B. Hursthousec, *Dalton Trans.*, 2006, 357.

31 T. Rojek, W. Goldeman, K. Ślepokura, W. Zierkiewicz and E. Matczak-Jon, *CrystEngComm*, 2019, **21**, 4340.

32 X. Huang, Z. Liu, C. Huang and Y. Wang, *Acta Crystallogr., Sect. E: Crystallogr. Commun.*, 2010, **66**, m59.

33 A. B. P. Lever, *Inorganic Electronic Spectroscopy*, Elsevier, New York, 1984.

34 J. Titiš, J. Hudák, J. Kožišek, A. Krutošiková, J. Moncol, D. Tarabová and R. Boča, *Inorg. Chim. Acta*, 2012, **388**, 106.

35 (*a*) H. Souissi and S. Kammoun, *Mater. Sci. Appl.*, 2011, **2**, 1121; (*b*) J. Titiš and R. Boča, *Inorg. Chem.*, 2011, **50**, 11838; (*c*) P. Diaz-Gallifa, O. Fabelo, J. Pasán, L. Canadillas-Delgado, F. Lloret, M. Julve and C. Ruiz-Pérez, *Inorg. Chem.*, 2014, **53**, 6299; (*d*) M. Gerloch and M. R. Manning, *Inorg. Chem.*, 1981, **20**, 1051.

36 J. L. Pascual, *Phys. Rev. B: Condens. Matter Mater. Phys.*, 2003, **67**, 115112.

37 M. Wildner, *J. Solid State Chem.*, 1995, **115**, 360.

38 M. Wildner, *Phys. Chem. Miner.*, 1996, **23**, 489.

39 (*a*) L. Y. Martin, C. R. Sperati and D. H. Busch, *J. Am. Chem. Soc.*, 1977, **99**, 2968; (*b*) J. C. Donini, B. R. Hollebone, G. London, A. B. P. Lever and J. C. Hempel, *Inorg. Chem.*, 1975, **14**, 455; (*c*) J. R. Perumareddi, *J. Phys. Chem.*, 1972, **76**, 3401.

40 R. Cortés, M. Drillon, X. Solans, L. Lezama and T. Rojo, *Inorg. Chem.*, 1997, **36**, 677.

41 C. G. Barraclough, A. K. Gregson and S. Mitra, *J. Chem. Phys.*, 1974, **60**, 962.

42 F. S. Delgado, N. Kerbellec, C. Ruiz-Pérez, J. Cano, F. Lloret and M. Julve, *Inorg. Chem.*, 2006, **45**, 1012.

43 F. Lloret, M. Julve, J. Cano, R. Ruiz-García and E. Pardo, *Inorg. Chim. Acta*, 2008, **361**, 3432.

44 R. Boča, *Struct. Bonding*, 2006, **117**, 1.

45 B. K. Tripuramallu, S. Mukherjee and S. K. Das, *Cryst. Growth Des.*, 2012, **12**, 5579.

46 J. Huang, P.-Y. Liu, H. Zhu, S.-S. Bao, L.-M. Zheng and J. Ma, *ChemPlusChem*, 2012, **77**, 1087.

47 N. Marino, O. F. Ikotun, M. Julve, F. Lloret, J. Cano and R. P. Doyle, *Inorg. Chem.*, 2011, **50**, 378.

48 (*a*) T. T. Wang, M. Ren, S.-S. Bao, B. Liu, L. Pi, Z.-S. Cai, Z.-H. Zheng, Z.-L. Xu and L.-M. Zheng, *Inorg. Chem.*, 2014, **53**, 3117; (*b*) T. T. Wang, M. Ren, S.-S. Bao, Z.-S. Cai, B. Liu, Z.-H. Zheng, Z.-L. Xu and L.-M. Zheng, *Dalton Trans.*, 2015, **44**, 4271.

49 (*a*) H. C. Yao, Y. Z. Li, S. Gao, Y. Song, L. M. Zheng and X. Q. Xin, *J. Solid State Chem.*, 2004, **177**, 4557; (*b*) B. Żurowska, A. Brzuszkiewicz and J. Ochocki, *Polyhedron*, 2008, **27**, 1721.